Int. J. Appl. Math. Comput. Sci., 2015, Vol. 25, No. 1, 189–201
DOI: 10.1515/amcs-2015-0014

SMAC–FDI: A SINGLE MODEL ACTIVE FAULT DETECTION AND ISOLATION SYSTEM FOR UNMANNED AIRCRAFT

GUILLAUME J.J. DUCARD [a]

[a] CNRS, I3S, UMR 7271
University of Nice Sophia Antipolis, 2000 Route des Lucioles, Bat. Euclide B, Les Algorithmes
06903 Sophia Antipolis, France
e-mail: ducard@i3s.unice.fr

This article presents a single model active fault detection and isolation system (SMAC-FDI) which is designed to efficiently detect and isolate a faulty actuator in a system, such as a small (unmanned) aircraft. This FDI system is based on a single and simple aerodynamic model of an aircraft in order to generate some residuals, as soon as an actuator fault occurs. These residuals are used to trigger an active strategy based on artificial exciting signals that searches within the residuals for the signature of an actuator fault. Fault isolation is carried out through an innovative mechanism that does not use the previous residuals but the actuator control signals directly. In addition, the paper presents a complete parameter-tuning strategy for this FDI system. The novel concepts are backed-up by simulations of a small unmanned aircraft experiencing successive actuator failures. The robustness of the SMAC-FDI method is tested in the presence of model uncertainties, realistic sensor noise and wind gusts. Finally, the paper concludes with a discussion on the computational efficiency of the method and its ability to run on small microcontrollers.

Keywords: fault detection and isolation, unmanned aerial vehicles, Kalman filtering, computationally efficient diagnosis system, active fault diagnosis, artificial excitation system.

1. Introduction

On-line fault diagnosis is an essential part of autonomous systems when safe operation and reliability are of primary concern. This is the case for unmanned aerial vehicles (UAVs) that perform missions in the vicinity of humans or infrastructures.

A reliable FDI system is necessary to assess the vehicle health status in order to decide on whether to continue the mission or to abort it as safe as possible. In addition, the information provided by such an FDI system may be used to overcome the presence of a fault in the system through a fault-tolerant control (FTC) architecture. Based on the on-line FDI outputs, the FTC system may be reconfigured or continuously adapted (Rodrigues *et al.*, 2007; Bonfè *et al.*, 2011), and thus increase significantly the overall operation range and safety (Blanke *et al.*, 2006; Theilliol *et al.*, 2008; Benini *et al.*, 2009).

Among the possible FDI techniques, a distinction can be made between those which are model based and others which are non-model based (Isermann, 2006; Alwi *et al.*, 2011). Still, most fault diagnosis approaches rely on a mathematical model of the plant being monitored (Simani *et al.*, 2003). The detection of a fault is achieved by assessing whether a "constructed signal" goes beyond a certain threshold. For example, such a "constructed signal" may be a residual, which is the deviation between the current hardware-measured value of a certain system-state variable and its expected value generated by the plant's model. However, other diagnosis signals may be constructed and evaluated (Isermann, 2006). There has been a lot of research on actuator-fault diagnosis and also some fewer works on sensor-fault diagnosis (e.g., Castaldi *et al.*, 2010). A list of techniques that are commonly encountered in the literature for the design of fault detection and isolation (FDI) systems can be found, e.g., in the works of Ducard (2009) and Alwi *et al.* (2011).

Designing a reliable FDI system is a challenging task, because it needs to provide an accurate evaluation of the systems' "health" despite external disturbances, model uncertainties, and sensor noise. Moreover, the FDI system has to be sensitive enough to detect faults without

triggering false alarms. Therefore, the robustness of the FDI system against the above-mentioned deficiencies is of particular concern. Examples of robustness analysis within the context of failure detection are provided, for example by Patton and Chen (1997), Zhang and Jiang (2000) as well as Belcastro and Chang (2002). In the work of Chen and Patton (1999), the robustness of FDI systems is enhanced by incorporating during the FDI-design phase the effects of disturbance signals, model uncertainties and measurement noise.

It is often the case that several model-based filters are organized in a bank in which one filter is sensitive to a specified failure but the other filters remain insensitive to that failure. Examples of this technique are (i) robust fault diagnosis for a spacecraft attitude control system (Patton *et al*., 2008), and (ii) the multiple model adaptive estimation (MMAE) method. This scheme is used to detect and isolate actuator or sensor faults on an aircraft by Magill (1965), Athans (1977), Maybeck and Stevens (1991), Eide and Maybeck (1996), Maybeck (1999), and Fekri *et al*. (2006).

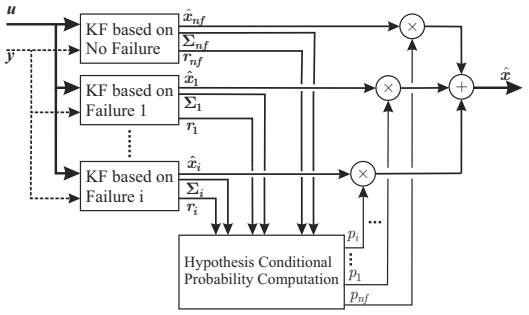

Fig. 1. Classical MMAE-FDI scheme.

As shown in Fig. 1, the classical MMAE-FDI scheme is based on a bank of parallel Kalman filters (KFs), each of which matches a particular fault status of the system, and is thus responsive for detecting deviations between model parameters and their true values. However, the MMAE method possesses three major limitations which are reported by Ducard and Geering (2008), who modified the MMAE method to compensate these limitations.

In this context, there are two families of fault detection and isolation systems, namely, passive FDI and active FDI systems. The former "wait" until a fault or failure occurs (Maybeck and Stevens, 1991; Maybeck, 1999), whereas the latter will artificially excite the aircraft, either by flying health check maneuvers (Elgersma *et al*., 1998; Azam *et al*., 2005), or by injecting test signals in the actuator commands and then assessing the individual health status of actuators and sensors (Elgersma and Glavaski, 2001; Campbell and Nikoukhah, 2004; Ducard and Geering, 2006; 2008; Boskovic *et al.*, 2007; Ducard, 2009; Bateman *et al.*, 2011).

This paper presents a new method that is inspired by the artificial actuator excitation mechanism used in conjunction with the EMMAE scheme as presented by Ducard and Geering (2006; 2008). Some fundamental differences, however, are that (i) the FDI system in this paper only employs a single EKF to generate residuals used for fault detection and trigger a fault alarm, and (ii) these residuals are then *not used* to assess the origin of the system's behavior discrepancy, but rather an active diagnostic procedure is engaged that artificially excites actuators and an additional stage performs fault isolation. Thus, the method presented in this paper is named a single model active fault detection and isolation system (SMAC-FDI).

Various variants of Kalman filters have been constructed for detecting and isolating faults or for state estimation and state reconstruction. The use of extended Kalman filters (EKFs) applied to nonlinear systems for FDI purposes has lately regained interest (Tanaka *et al*., 2006; Ducard and Geering, 2008). Campbell *et al*. (2007) discuss the implementation of a sigma point filter (SPF) which was originally introduced as the unscented Kalman filter (UKF), where the distributions are approximated by a finite set of points. It is used to estimate aircraft states and aerodynamic derivatives in real time. This is a nonlinear estimation algorithm that can be performed on-line, which possesses robustness properties against parameter uncertainties, filter tuning and initial conditions.

However, all of the techniques described above are computationally quite demanding. The FDI system of this paper is designed with three main requirements: (i) to use a single model, as simple as possible, of the aircraft, whose actuators are to be monitored, (ii) to require very low computational effort, so that the algorithm can run on a small microcontroller, (iii) to be robust to model uncertainties, sensor noise and external perturbation. A first version of this SMAC-FDI system was presented by Ducard and Geering (2010) and improved by Ducard (2013).

The main contributions of this article are to (i) present an innovative architecture of an FDI system based on a single filter for the generation of residuals independently of the actuator fault scenario, (ii) describe an active strategy that searches in the generated residuals for the signature of an actuator fault and test the actuators in a systematic way, (iii) present an actuator-fault isolation procedure that is not based on residuals' manipulations but on the direct observation of control signals only, (iv) provide some tuning guidelines for the parameters involved in this FDI system, (v) show that the SMAC-FDI method is highly computationally efficient, and therefore, can run on microcontrollers with low computational resources, and (vi) demonstrate the performance of this simple method in simulation and despite the presence of

model uncertainties.

The article continues with briefly recalling the aircraft model used throughout this work.

2. System configuration and dynamics

2.1. Aircraft configuration. The five control surfaces of the aircraft under consideration are one left aileron, one right aileron, one left elevator, one right elevator, and one rudder as shown in Fig. 2. All actuators are fully independent. The control vector for the aircraft involving only actuator deflections is thus

$$\boldsymbol{\delta} = [\delta_{a_1} \quad \delta_{a_2} \quad \delta_{e_1} \quad \delta_{e_2} \quad \delta_r]^\top .$$

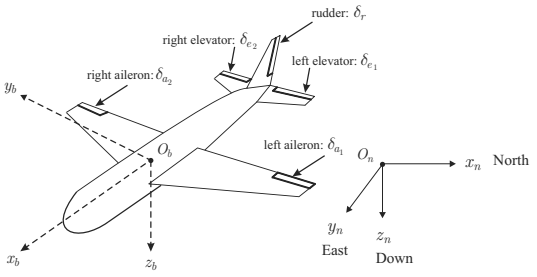

Fig. 2. Aircraft actuator configuration.

2.2. Aircraft nonlinear dynamics. For the design of the filter which is the core of the FDI system suggested in this paper, the equation for the dynamics of the turn rates is considered. The explicit relationship between the turn-rate vector $\boldsymbol{\omega} = [p\ q\ r]^\top$, with the roll, pitch and yaw rates denoted by p, q, r, respectively, the inertia matrix $\boldsymbol{I}^b$ and the torques applied to the aircraft, i.e., $\boldsymbol{\Gamma} = [L\ M\ N]^\top$, expressed in the body-axes frame (x_b, y_b, z_b) of the aircraft, is as follows:

$$\dot{\boldsymbol{\omega}} = (\boldsymbol{I}^b)^{-1}\left(\boldsymbol{\Gamma} - \boldsymbol{\omega} \times \boldsymbol{I}^b\boldsymbol{\omega}\right). \tag{1}$$

The aerodynamic moments of the small aircraft of this work are modeled as in the work of Möckli (2006) and Ducard (2009):

$$\begin{aligned} L &= \bar{q}SbC_L(\delta_{a1}, \delta_{a2}, \delta_{e1}, \delta_{e2}, p, r, \beta)\ , \\ M &= \bar{q}S\bar{c}C_M(\delta_{a1}, \delta_{a2}, \delta_{e1}, \delta_{e2}, \alpha, q)\ , \\ N &= \bar{q}SbC_N(\delta_{a1}, \delta_{a2}, \delta_{e1}, \delta_{e2}, \delta_r, r, \beta)\ , \end{aligned} \tag{2}$$

where the dynamic pressure is $\bar{q} = \rho V_T^2/2$, the total airspeed of the aircraft is V_T, the air density is ρ, and the other parameters are summarized in Table A1, whereas details regarding the measurement system part of the FDI system are summarized in Table 1.

The aerodynamic derivatives are expressed as a linear combination of the state elements and control inputs as

$$\begin{aligned} C_L &= C_{L_{a1}}\delta_{a1} + C_{L_{a2}}\delta_{a2} + C_{L_{e1}}\delta_{e1} + C_{L_{e2}}\delta_{e2} \\ &\quad + C_{L\tilde{p}}\tilde{p} + C_{L\tilde{r}}\tilde{r} + C_{L\beta}\beta\ , \\ C_M &= C_{M1} + C_{M_{a1}}\delta_{a1} + C_{M_{a2}}\delta_{a2} + C_{M_{e1}}\delta_{e1} \\ &\quad + C_{M_{e2}}\delta_{e2} + C_{M\tilde{q}}\tilde{q} + C_{M\alpha}\alpha\ , \\ C_N &= C_{N_{\delta r}}\delta_r + C_{N\tilde{r}}\tilde{r} + C_{N\beta}\beta\ , \end{aligned}$$

with

$$\tilde{p} = \frac{bp}{2V_T}\ , \quad \tilde{q} = \frac{\bar{c}q}{2V_T}\ , \quad \tilde{r} = \frac{br}{2V_T}\ .$$

The last two differential equations concern the angle of attack α and the sideslip angle β as follows (see the work of Ducard (2009) for derivation):

$$\begin{aligned} \dot{\alpha} &\approx q + \frac{g}{V_T}\left\{1 + \frac{\bar{q}S}{mg}([C_{X1} + C_{Z\alpha}]\alpha + C_{Z1})\right\}\ , \\ \dot{\beta} &\approx -r + \frac{\bar{q}SC_{Y1}}{mV_T}\beta\ . \end{aligned} \tag{3}$$

3. Actuator fault detection and isolation

Figure 3 shows the architecture of the SMAC-FDI system and its four main components, which are detailed subsequently.

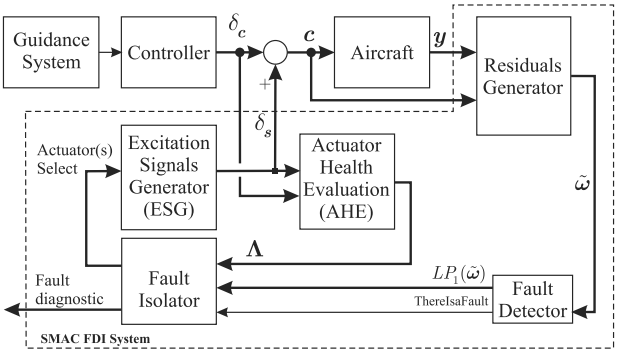

Fig. 3. Architecture of the SMAC-FDI system.

3.1. Residual generator. The residual generator monitors the control signals sent to the actuators and the behavior of the aircraft through the reading of selected measurement of the aircraft's dynamics. In the SMAC-FDI system, the turn rates p, q, and r are measured and compared with the expected turn rates $\hat{p}$, $\hat{q}$, and $\hat{r}$, respectively, which are obtained using a model of the aircraft. This model receives the same actuator commands as the real aircraft. A filter is used to take into account model uncertainties and sensor measurement data noise. This filter is an EKF, whose useful output (for the FDI

purpose) is the vector of residuals $\tilde{\boldsymbol{\omega}}_k$ defined as follows

$$\tilde{\boldsymbol{\omega}}_k = \boldsymbol{y}_k - \hat{\boldsymbol{x}}_{k|k-1} = \begin{bmatrix} \tilde{p} \\ \tilde{q} \\ \tilde{r} \end{bmatrix}_k = \begin{bmatrix} p_k - \hat{p}_{(k|k-1)} \\ q_k - \hat{q}_{(k|k-1)} \\ r_k - \hat{r}_{(k|k-1)} \end{bmatrix}_k ,$$

where the measurement vector at the discrete-time instant k is $y_k = [p_k \;\; q_k \;\; r_k]^\top$, and the filter's state vector is the estimate of the turn rates. These residuals indicate whether the aircraft has dynamics that deviate from the model-expected dynamics. If the residual values are higher than a certain threshold, it is most likely that an actuator fault is present in the system. The equations of the EKF used in this residual generator are well known but briefly recalled here below for completeness (Brown and Hwang, 1997).

3.1.1. Filter equations.

1. The Kalman gain matrix $\boldsymbol{L}_k$ is computed as $\boldsymbol{L}_k = \boldsymbol{\Sigma}_{k|k-1}\boldsymbol{H}_k^T \left[\boldsymbol{H}_k\boldsymbol{\Sigma}_{k|k-1}\boldsymbol{H}_k^T + \boldsymbol{R}_{v,k}\right]^{-1}$, where the last propagated state-error covariance matrix is $\boldsymbol{\Sigma}_{k|k-1}$, the measurement noise covariance matrix is $\boldsymbol{R}_{v,k}$ and the measurement matrix is $\boldsymbol{H}_k = \boldsymbol{I}_3$.

2. The measurement update of the state estimate is $\hat{\boldsymbol{x}}_{k|k} = \hat{\boldsymbol{x}}_{k|k-1} + \boldsymbol{L}_k[\boldsymbol{y}_k - \hat{\boldsymbol{x}}_{k|k-1}]$, where the last extrapolated state estimate is $\hat{\boldsymbol{x}}_{k|k-1}$.

3. The update of the state-error covariance matrix is $\boldsymbol{\Sigma}_{k|k} = \boldsymbol{E}\{\boldsymbol{e}_{k|k}\boldsymbol{e}_{k|k}^T\}$ with $\boldsymbol{e}_{k|k} = \boldsymbol{x}(k) - \hat{\boldsymbol{x}}_{k|k}$, where $\boldsymbol{x}(k)$ is the true (unknown) value of the state vector at the discrete instant k. The matrix $\boldsymbol{\Sigma}_{k|k}$ is recursively computed as $\boldsymbol{\Sigma}_{k|k} = [\boldsymbol{I} - \boldsymbol{L}_k\boldsymbol{H}_k]\,\boldsymbol{\Sigma}_{k|k-1}$.

4. The forward propagation of the state error covariance matrix is $\boldsymbol{\Sigma}_{k+1|k} = \boldsymbol{\phi}_k\boldsymbol{\Sigma}_{k|k}\boldsymbol{\phi}_k^T + \boldsymbol{R}_{w,k}$, where the matrix $\boldsymbol{R}_{w,k}$ represents the covariance of the discrete process noise on the elements of the state vector.

5. The state-estimate propagation step is done with $\hat{\boldsymbol{x}}_{k+1|k} = \hat{\boldsymbol{x}}_{k|k} + \dot{\hat{\boldsymbol{x}}}_{k|k}T_s$, where the time derivative of the state $\dot{\hat{\boldsymbol{x}}}_{k|k} = \boldsymbol{f}\left(\hat{\boldsymbol{x}}_{k|k}, \boldsymbol{u}_k\right)$ is obtained by direct calculation of Eqn. (1).

3.1.2. Discrete transition matrix. The discrete transition matrix $\boldsymbol{\phi}_k$ is computed as $\boldsymbol{\phi}_k = \boldsymbol{I_3} + \boldsymbol{F}(k)T_s$. The continuous transition matrix $\boldsymbol{F}(k) \in \mathbb{R}^{3\times3}$ is obtained using the model of the aircraft described in Section 2 and updated at each sample time by the estimates of the turn rates $\hat{p}_{(k|k)}$, $\hat{q}_{(k|k)}$, $\hat{r}_{(k|k)}$ and with the measurement data for the airspeed V_T involved in the dynamic pressure $\bar{q} = \frac{1}{2}\rho {V_T}^2$ as follows:

$$\boldsymbol{F}(k) = \begin{bmatrix} A_{11\overline{q}}\,\overline{q} + A_{11q}\,q & A_{12p}\,p + A_{12r}\,r \\ A_{21p}\,p + A_{21r}\,r & A_{22\overline{q}}\,\overline{q} \\ A_{31\overline{q}}\,\overline{q} + A_{31q}\,q & A_{32p}\,p + A_{32r}\,r \\ A_{13\overline{q}}\,\overline{q} + A_{13q}\,q \\ A_{23p}\,p + A_{23r}\,r \\ A_{33\overline{q}}\,\overline{q} + A_{33q}\,q \end{bmatrix},$$

with each term of $\boldsymbol{F}(k)$ being evaluated at the current estimated operating point given by $p = \hat{p}_{(k|k)}$, $q = \hat{q}_{(k|k)}$, $r = \hat{r}_{(k|k)}$ and $\bar{q} = \bar{q}_{(k)}$. The terms of the transition matrix are defined as follows:

$$\begin{aligned}
A_{11\overline{q}} &= \frac{I_{zz}Sb^2C_{L\bar{p}}}{2D_1V_T}, \\
A_{11q} &= A_{12p} = \frac{-N_1}{D_1}, \\
A_{12r} &= A_{13q} = \frac{I_{yy}I_{zz} - I_{xz}^2 - I_{zz}^2}{D_1}, \\
A_{13\overline{q}} &= \frac{Sb^2[I_{zz}C_{L\bar{r}} - I_{xz}C_{N\bar{r}}]}{2D_1V_T}, \\
A_{21r} &= A_{23p} = \frac{I_{zz} - I_{xx}}{I_{yy}}, \\
A_{21p} &= -A_{23r} = \frac{2I_{xz}}{I_{yy}}, \\
A_{22\overline{q}} &= \frac{S\,\overline{c}^2\,C_{M\bar{q}}}{2V_TI_{yy}}, \\
A_{31q} &= \frac{I_{xx}^2 - I_{xx}I_{yy} + I_{xz}^2}{D_1}, \\
A_{31\overline{q}} &= -\frac{I_{xz}Sb^2C_{L\bar{p}}}{2D_1V_T}, \\
A_{32q} &= A_{31p}, \\
A_{33\overline{q}} &= \frac{Sb^2[I_{xx}C_{N\bar{r}} - I_{xz}C_{L\bar{r}}]}{2D_1V_T}, \\
A_{32r} &= A_{33q} = \frac{N_1}{D_1},
\end{aligned}$$

using the auxiliary constants $D_1 = I_{xx}I_{zz} - {I_{xz}}^2$ and $N_1 = I_{xz}(I_{xx} - I_{yy} + I_{zz})$, taking into account $I_{xz} = I_{zx}$.

3.1.3. Process noise covariance matrix. The value of $\boldsymbol{R}_{w,k}$ is found from the continuous process noise covariance matrix $\boldsymbol{R}_w$ and the continuous transition matrix $\boldsymbol{\phi}$ according to

$$\begin{aligned}
\boldsymbol{R}_{w,k} &= \int_0^{T_s} \boldsymbol{\phi}(\tau)\boldsymbol{R}_w\boldsymbol{\phi}^\top(\tau)\,\mathrm{d}\tau, \\
\boldsymbol{R}_w &= E(\boldsymbol{w}\boldsymbol{w}^\top) = \mathrm{diag}(w_1^2, w_2^2, w_3^2), \\
\boldsymbol{w} &= [w_1, w_2, w_3]^\top, \quad E(w_iw_j) = 0, \quad \forall i \neq j\ ,
\end{aligned} \tag{4}$$

where the process-noise vector acting on the state vector dynamics is $\boldsymbol{w}$. The matrix $\boldsymbol{R}_{w,k} \in \mathbb{R}^{3\times3}$ is symmetric and the lower-triangle terms are obtained as follows:

$$\boldsymbol{R}_{w,k}(1,1) = w_1^2 T_s \left[1 + \boldsymbol{\phi}_{(1,1)} T_s + \boldsymbol{\phi}_{(1,1)}^2 \frac{{T_s}^2}{3}\right] + \frac{{T_s}^3}{3}\left[{w_2}^2 \boldsymbol{\phi}_{(1,2)}^2 + {w_3}^2 {\phi_{(1,3)}}^2\right],$$

$$\boldsymbol{R}_{w,k}(2,2) = w_2^2 T_s \left[1 + \boldsymbol{\phi}_{(2,2)} T_s + \boldsymbol{\phi}_{(2,2)}^2 \frac{{T_s}^2}{3}\right] + \frac{{T_s}^3}{3}\left[{w_1}^2 \boldsymbol{\phi}_{(2,1)}^2 + {w_3}^2 {\phi_{(2,3)}}^2\right],$$

$$\boldsymbol{R}_{w,k}(3,3) = w_3^2 T_s \left[1 + \boldsymbol{\phi}_{(3,3)} T_s + \phi_{(3,3)}^2 \frac{{T_s}^2}{3}\right] + \frac{{T_s}^3}{3}\left[{w_1}^2 \boldsymbol{\phi}_{(3,1)}^2 + {w_2}^2 {\boldsymbol{\phi}_{(3,2)}}^2\right],$$

$$\boldsymbol{R}_{w,k}(2,1) = A_1 \boldsymbol{\phi}_{(2,1)} + A_2 \boldsymbol{\phi}_{(1,2)} + {w_3}^2 \frac{{T_s}^3}{3} \boldsymbol{\phi}_{(1,3)} \boldsymbol{\phi}_{(2,3)},$$

$$\boldsymbol{R}_{w,k}(3,1) = A_1 \boldsymbol{\phi}_{(3,1)} + A_3 \boldsymbol{\phi}_{(1,3)} + {w_2}^2 \frac{{T_s}^3}{3} \boldsymbol{\phi}_{(1,2)} \boldsymbol{\phi}_{(3,2)},$$

$$\boldsymbol{R}_{w,k}(3,2) = A_2 \boldsymbol{\phi}_{(2,1)} + A_3 \boldsymbol{\phi}_{(2,3)} + {w_1}^2 \frac{{T_s}^3}{3} \boldsymbol{\phi}_{(2,1)} \boldsymbol{\phi}_{(3,1)},$$

with the constants

$$A_1 = {w_1}^2 \frac{{T_s}^2}{2}\left[1 + \frac{2}{3} T_s \phi_{(1,1)}\right],$$

$$A_2 = {w_2}^2 \frac{{T_s}^2}{2}\left[1 + \frac{2}{3} T_s \phi_{(2,2)}\right],$$

$$A_3 = {w_3}^2 \frac{{T_s}^2}{2}\left[1 + \frac{2}{3} T_s \phi_{(3,3)}\right],$$

where $\boldsymbol{\phi}_{(i,j)}$ and $\boldsymbol{R}_{w,k}(i,j)$ designate the terms found at the i-th line and the j-th column of the matrix $\boldsymbol{\phi}$ and matrix $\boldsymbol{R}_{w,k}$, respectively.

3.1.4. Sensor noise and filter tuning. The measurement vector involved in the EKF of the SMAC-FDI system is $\boldsymbol{y} = [p,\, q,\, r]^\top$, where the body-axis turn rates p, q, and r are measured by gyrometers. The measurement noise is assumed to be Gaussian distributed with zero mean. The noise standard deviations are $\sigma_{pqr} = 0.08\,[\text{rad/s}]$ (variance $\Sigma_{pqr} = 0.0064\,[\text{rad/s}]^2$) for the turn rates measured by three identical gyrometers, each on its respective body axis.

In order to build these residuals, the Kalman filter uses a model of the aircraft's turn rate dynamics. However, this model contains parameters which are uncertain. In order to cope with uncertainties, the Kalman filter possesses intrinsically a mechanism to compute the observer gain matrix (Kalman gain) that mitigates the confidence level between the quality of the model (through the process noise covariance matrix $\boldsymbol{R}_w$) and the quality of the measurement data (through the measurement noise covariance matrix $\boldsymbol{R}_v$).

In this work, the filter is initialized with the initial state estimate $\hat{\boldsymbol{x}}_{0|-1} = [0\ 0\ 0]^\top$ and initial state error covariance matrix $\Sigma_{0|-1} = \boldsymbol{I}_3$. The EKF is tuned by selecting the measurement noise covariance matrix $\boldsymbol{R}_v = 0.1 \times \boldsymbol{I}_3\,[\text{rad/s}]^2$ whose values are chosen higher than those of the sensor characteristics mentioned above.

The process noise covariance matrix is chosen to be sufficiently large (in this case, for example, $\boldsymbol{R}_w = 2 \times \boldsymbol{I}_3\,[\text{rad/s}]^2$) to ensure the proper convergence of the filter in nominal conditions, as may be understood from the condition in Eqn. (10). From a practical point of view, it is interesting to note that (i) increasing the process noise makes the amplitude of the residuals larger, and (ii) better results are obtained when the terms of $\boldsymbol{R}_w$ are larger than those of $\boldsymbol{R}_v$.

3.2. Fault detector.

3.2.1. Architecture of the fault detector. The success of fault detection is dependent on the possibility to create relevant signals that deviate from a nominal value in the case of a fault. In this work, the residuals of the Kalman filter are used and assembled as shown in Fig. 4. First, the vector of turn rate residuals $\tilde{\boldsymbol{\omega}}$ coming from the EKF is filtered by a first-order low-pass filter LP_1 with a cut-off frequency f_1. Second, the residuals are assembled as follows:

$$\Gamma_1 = |LP_1(\tilde{p})| + |LP_1(\tilde{q})| + |LP_1(\tilde{r})|\,. \tag{5}$$

Third, the integrating effect of the first-order low-pass filter with cut-off frequency f_2 is used to transform the signal Γ_1 into the signal Γ_2. Fourth, if the signal Γ_2 exceeds the threshold value $\Gamma_{2,\text{thresh}}$, the fault detector indicates that there is a fault somewhere in the system by setting to "1" the output signal labeled "ThereIsaFault", shown in Fig. 4. The origin of the fault is not known at this stage. It is the task of the fault isolator subsystem in Section 3.5 to investigate the origin of the fault.

3.2.2. Tuning of the low-pass filters. As shown in Fig. 4, two low-pass filters are used, namely, LP1 and LP2. Their purpose is to attenuate oscillations in the residuals when excitation signals δ_s are used during a fault isolation process. As shown in Section 3.3, these excitation signals are of sinusoidal form with a fixed frequency of 1 Hz (in this work). Thus, the cut-off frequencies f_1 and f_2 are

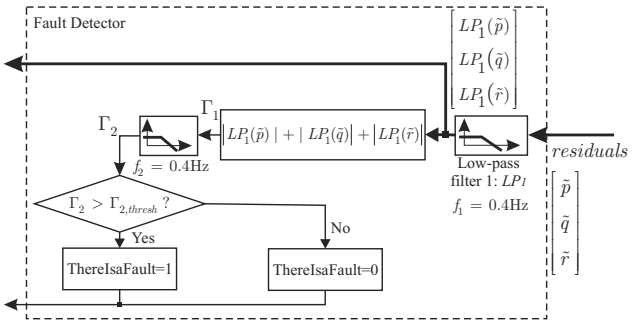

Fig. 4. Architecture of the fault detector subsystem.

both chosen is the range $]0, 1[$ Hz. They were chosen as $f_1 = f_2 = 0.4$ Hz, which provides a trade-off between smoothing and delaying the residual signals.

3.2.3. Threshold value $\Gamma_{2,\mathrm{thresh}}$. For the determination of a suitable value for $\Gamma_{2,\mathrm{thresh}}$, a linear SISO model is constructed for the roll, pitch and yaw axis as follows:

$$\dot{\chi} = (\hat{a}_\chi + \Delta a_\chi)\,\chi + \left(\hat{b}_\chi + \Delta b_\chi\right)\delta_\chi, \tag{6}$$

where the variable χ is p, q, r, respectively, and the real control input to the system δ_χ (that may include a fault) is δ_a, δ_e, δ_r, respectively. Note that (6) is used as a template for three different equations.

The terms $\hat{a}_\chi$ and $\hat{b}_\chi$ represent the uncertain model parameters in use in the FDI system. The "true values" a_χ and b_χ are the sum of the model terms and their respective uncertainty part Δa_χ and Δb_χ as follows:

$$a_\chi = \hat{a}_\chi + \Delta a_\chi, \qquad b_\chi = \hat{b}_\chi + \Delta b_\chi\ . \tag{7}$$

For analytical purposes, let us consider a linear Kalman-type estimator of the form

$$\dot{\hat{\chi}} = \hat{a}_\chi \hat{\chi} + \hat{b}_\chi \delta_{\chi,\,c} + L_\chi(\chi - \hat{\chi}), \tag{8}$$

where the Kalman gain is L_χ and the control signal generated by the flight controller is $\delta_{\chi,c}$. By substracting (8) from (6), the differential equation for the residuals of turn-rate dynamics is obtained as follows:

$$\dot{\tilde{\chi}} = -(L_\chi - \hat{a}_\chi)\tilde{\chi} + \hat{b}_\chi \Delta\delta_\chi + \Delta\epsilon(\chi(t), x(t)), \tag{9}$$

where the term $\Delta\delta_\chi = \delta_\chi - \delta_{\chi,\,c}$ is the deviation between a true actuator position and its commanded value. All of the uncertainty contributions are regrouped in the term $\Delta\epsilon(\chi(t), x(t))$, which may be dependent on the turn rate itself $\chi(t)$ and other state elements, such as the angle of attack α, the sideslip angle β and the aircraft total airspeed V_T. The stability of the filter is obtained if the condition

$$L_\chi - \hat{a}_\chi > 0 \tag{10}$$

is satisfied, in which case the residual $\tilde{\chi}$ converges to a certain value if the system approaches steady-state conditions. This condition is fulfilled if the terms in $\boldsymbol{R_w}$ are chosen sufficiently large.

In the presence of model uncertainties or actuator faults, the residuals will no longer be zero-mean centered. This is precisely what will trigger the detection of a fault in the system. Therefore, it is necessary to be able to assess the amount of bias in the residuals that is due to model uncertainties.

To this end, suppose that an actuator failure occurs; the flight controller will compensate it by actuating the remaining actuators in order to stabilize the turn rates of the vehicle, i.e., $p = q = r = 0$. Moreover, if the vehicle is flying straight, at constant level and speed, the terms $\Delta\delta_\chi$ and $\Delta\epsilon$ will reach constant values $\Delta\delta_{\chi,ss}$ and $\Delta\epsilon_{ss}$, respectively. Therefore, the residual in (9) reaches the following steady-state value:

$$\tilde{\chi}_{ss} = \frac{\hat{b}_\chi \Delta\delta_{\chi,ss} + \Delta\epsilon_{ss}}{L_\chi - \hat{a}_\chi} = \frac{\hat{b}_\chi\,(\Delta\delta_{\chi,ss} + \Delta\gamma_{ss})}{L_\chi - \hat{a}_\chi}, \tag{11}$$

with $\Delta\gamma_{ss} = \Delta\epsilon_{ss}/\hat{b}_\chi$. Once the maximum amount of uncertainty in the model, $\sup|\Delta\epsilon|$, is specified, the threshold value $\Gamma_{2,\,\mathrm{thresh}}$ of the signal Γ_2 is chosen according to the following inequality:

$$\begin{aligned}\frac{\hat{b}_\chi \sup|\Delta\gamma|}{L_\chi - \hat{a}_\chi} &< \Gamma_{2,\,\mathrm{thresh}} \\ &< \frac{\hat{b}_\chi\,(|\Delta\delta_{\chi,\min}| - \sup|\Delta\gamma|)}{L_\chi - \hat{a}_\chi}.\end{aligned} \tag{12}$$

Remark 1.

- The results shown in Section 4 are obtained with a constant value of $\Gamma_{2,\,\mathrm{thresh}} = 0.025$ rad/s. However, an adaptive value of $\Gamma_{2,\,\mathrm{thresh}}$ can be computed on-line based on Eqn. (12) to take into account the current flight conditions.
- If the value of the true model term b_χ is known within some uncertainty bounds $\hat{b}_\chi = b_\chi \pm \Delta b_\chi$, in the FDI system it is better to choose an overestimated value for $\hat{b}_\chi$, i.e., $\hat{b}_\chi = b_\chi + |\Delta b_\chi|$, as this tends to increase the ratio between: (a) the detectable fault-amplitude level and (b) the uncertainty level.

3.2.4. Effect of model uncertainties on actuator fault detection performance. The effect of model uncertainties on the minimum detectable value of the actuator fault $\Delta\delta_{\chi,\min}$ is visible in (12), where it appears that a lower bound for $\Delta\delta_{\chi,\min}$, given the maximum uncertainty level $\sup|\Delta\gamma|$, is

$$|\Delta\delta_{\chi,\min}| > 2\sup|\Delta\gamma|\ . \tag{13}$$

Clearly, the actuator-fault amplitude that can be detected is bounded from below by the amount of uncertainty in the model.

3.3. Excitation signals generator (ESG). As shown in Fig. 3, the fault isolator selects which actuator the ESG is to test. The ESG superimposes on the selected actuator's input an artificial excitation signal of the form

$$\delta_s(t) = A\sin(\omega t). \tag{14}$$

The frequency ω has to be chosen within the bandwidth of the aircraft considered. Indeed, as explained in Section 3.4, the excitation signal must be of sufficiently low frequency such that the aircraft dynamics get disturbed by this excitation signal. As a result, the flight controller will generate actuator commands to compensate this perturbation. If the presence of this excitation signal is visible in the actuator control signals, this means that the tested actuator has actually not failed, and vice versa.

In order to discuss a suitable value for the amplitude A, let us consider the dynamics of the residuals when the control signal δ_s is applied to a failed actuator. The dynamics of the residual vector $\tilde{\chi}$ are as follows:

$$\dot{\tilde{\chi}} = -(L_\chi - \hat{a}_\chi)\tilde{\chi} + \hat{b}_\chi\left(\Delta\delta_\chi - A\sin\omega t + \Delta\gamma\right) . \tag{15}$$

It can be shown that the asymptotic solution to (15) is

$$\tilde{\chi}_\infty = C_1 - C_2\sin(\omega t - \phi_0), \tag{16}$$

with the terms

$$C_1 = \frac{\hat{b}_\chi}{L_\chi - \hat{a}_\chi}\left(\Delta\delta_\chi + \Delta\gamma\right),$$

$$C_2 = \frac{\hat{b}_\chi A}{\sqrt{\omega^2 + (L_\chi - \hat{a}_\chi)^2}},$$

and

$$\phi_0 = \tan^{-1}\left(\frac{\omega}{L_\chi - \hat{a}_\chi}\right).$$

In the presence of an actuator fault in the system, it is shown in Fig. 4 that the signal Γ_2 must exceed a certain threshold $\Gamma_{2,\mathrm{thresh}}$ for the fault to be detected. The signal Γ_2 is obtained by low-pass filtering the signal Γ_1. In order to simplify the discussion, let us assume that the signal $\Gamma_1 = |\tilde{\chi}|$, which is the case when the residuals build up dominantly on a certain aircraft axis.

In view of (16), it can be shown that the mean value of Γ_2 is mostly given by the "constant" part of $|\tilde{\chi}|$, i.e., C_1. As soon as the excitation signal is triggered, additional calculations show that irrespective of the amplitude of C_2 compared with C_1, ($C_2 > C_1$ or $C_2 < C_1$), the condition $\Gamma_2 > \Gamma_{2,\mathrm{thresh}}$, which triggered the excitation signal, still remains satisfied after the addition of excitation signals. In fact, if the term C_1 is smaller than C_2, the excitation term has the positive effect of contributing to a higher value of Γ_2.

Therefore, the amplitude A is chosen as a compromise between (i) a value of A as large as possible such that the fault isolation explained in Section 3.4 can maximize the amplitude of the isolation signals Λ_i, despite the possible presence of external perturbation, such as wind gusts or aircraft maneuvers, thus improving FDI robustness, and (ii) a sufficiently small value of A, so as not to unnecessarily destabilize the aircraft as it flies if the excitation signal is applied to a non-failed actuator.

Remark 2. In Section 4, the results shown are obtained with a frequency $\omega = 2\pi$ [rad/s] and an amplitude $A = 2\pi/180$ [rad].

3.4. Actuator health evaluator (AHE). The actuator health evaluator (AHE) is responsible for assessing whether a selected actuator δ_i is properly functioning. As shown in Fig. 3, the AHE module receives the control signals $\boldsymbol{\delta_c} = [\delta_{c,1}\ldots\delta_{c,n}]$ of n actuators generated by the flight controller and the excitation signals $\boldsymbol{\delta_s} = [\delta_{s,1}\ldots\delta_{s,n}]$ generated by the ESG module.

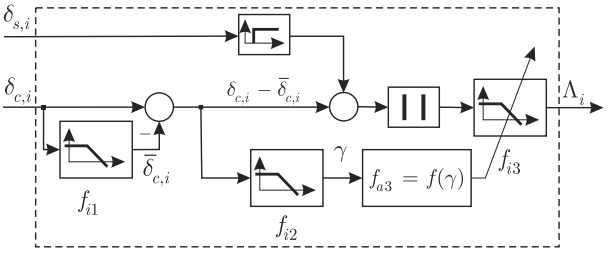

Fig. 5. Architecture of the i-th actuator health evaluator, AHE subsystem.

For the i-th actuator, the output of the AHE is given by the following equation:

$$\Lambda_i(k) = LP_{i3}\left(\left|\delta_{s,i}(k - \lambda T_s) + [\delta_{c,i} - \overline{\delta}_{c,i}](k)\right|\right), \tag{17}$$

where $LP_{i3}(X)$ means that the signal X is filtered through a first-order low-pass filter $1/(1+\tau_{i3}s)$ with cut-off frequency $f_{i3} = 1/2\pi\tau_{i3}$ [Hz]. The choice of the frequency f_{i3} is not that important, as its value is decreased if the signal γ gets small and below a certain threshold, and vice versa. This low-pass filter is only meant to attenuate the noise level of its incoming signal. In steady-state conditions, the signal $\overline{\delta}_{c,i}$ equals the mean value of $\delta_{c,i}$. The excitation signal $\delta_{s,i}$ is delayed by an integer number of sampling periods λT_s, $\lambda \in \mathbb{N}^+$, such that the signals $[\delta_{c,i} - \overline{\delta}_{c,i}](k)$ and $\delta_{s,i}(k - \lambda T_s)$ are in opposite phase when Actuator i is non-failed. The delay λ is determined experimentally and corresponds to the delay of the flight controller to react to the disturbance caused by $\delta_{s,i}$ superimposed onto Actuator i when non-failed. For

a better understanding, let us consider the following two cases (Ducard and Geering, 2010).

3.4.1. Case 1: Testing a failed actuator. If Actuator i being tested has really failed, the excitation signal $\delta_{s,i}$ has no effect on the control signal $\delta_{c,i}$ but has an effect on the residuals generated by the residual generator. The AHE detects the non-response of the flight controller to the excitation $\delta_{s,i}$ and thus generates the signal Λ_i whose amplitude is compared with a threshold value (Ail1FaultThresh, Ail2FaultThresh, Elev1FaultThresh, Elev2FaultThresh, and RuddFaultThresh, respectively) inside the fault isolator. If Λ_i is above the threshold, Actuator i is declared faulty, as shown in Figs. 9 and 10.

3.4.2. Case 2: Testing a non-failed actuator. If Actuator i has actually not failed, the superimposed excitation signal $\delta_{s,i}$ has influence on the aircraft dynamics and the flight controller will try to compensate the disturbance input signal. However, there is a small delay in the controller response. The term $\delta_{s,i}$ is delayed in such a way so as to be in opposite phase with the term $[\delta_{c,i} - \overline{\delta}_{c,i}]$. Therefore, their sum Λ_i is close to zero and below the threshold value (Ail1FaultThresh, Ail2FaultThresh, Elev1FaultThresh, Elev2FaultThresh, and RuddFaultThresh, respectively) in the fault isolator module. Actuator i is thus declared non-faulty, as shown in Figs. 9 and 10.

3.4.3. Tuning of the AHE. The tuning of the AHE subsystem consists in finding the appropriate cut-off frequency denoted by f_{i1}, as shown in Fig. 5. The frequency f_{i1} is chosen in such a way that the term $\overline{\delta}_{c,i}$ converges to the mean value of $\delta_{c,i}$, $E(\delta_{c,i})$, after a time interval ΔT:

$$\left| \frac{E(\delta_{c,i}) - \overline{\delta}_{c,i}(t > \Delta T)}{E(\delta_{c,i})} \right| < \epsilon \,, \tag{18}$$

with the relative error $\epsilon = 5\%$, for example. The frequency f_{i1} is chosen as

$$f_{i1} > \frac{\ln(1/\epsilon)}{2\pi \Delta T}. \tag{19}$$

3.4.4. Selection of the threshold values for actuator fault diagnosis. The threshold values (Ail1FaultThresh, Ail2FaultThresh, Elev1FaultThresh, Elev2FaultThresh, RuddFaultThresh) are used inside the fault isolator module (Section 3.5) to declare an actuator to have failed.

The signal Λ_i at the output of the i-th AHE subsystem has a value close to zero in the non-fault case and a maximum value of

$$\Lambda_{i,\max} = \frac{2A}{\pi} \tag{20}$$

if Actuator i experiences a complete failure case. If Actuator i experiences a fault, such as a loss of effectiveness, the signal Λ_i takes an intermediate value within the range $0 < \Lambda_i < 2A/\pi$.

Example 1. The simulations provided in Section 4 have been performed with $A = 2\pi/180$ [rad]. According to (20), during the complete failure of Aileron1 and Aileron2, the values of Λ_1 and Λ_2 should be 0.022 [rad], which is confirmed by the results shown in Fig. 9. Therefore, the threshold values for actuator fault diagnosis are chosen to be $\Lambda_{i,\text{thresh}} = 0.01$ [rad]. ♦

3.5. Fault isolator. The complete architecture of the fault isolator is detailed in Fig. 6. It manipulates the residuals in order to choose which actuator group to test (the aileron group, the elevator group or the rudder group). In each of these groups the fault isolator selects an actuator to test. It is the responsibility of the ESG subsystem shown in Fig. 3 to generate the artificial excitation signals to superimpose on the selected actuator. The threshold values $\tilde{p}_{\text{thresh}}$, $\tilde{q}_{\text{thresh}}$ and $\tilde{r}_{\text{thresh}}$ that appear in Fig. 6 are chosen according to (12) for each axis. For example, in the following simulations, $\tilde{p}_{\text{thresh}} = 0.03$ [rad], $\tilde{q}_{\text{thresh}} = 0.2$ [rad] and $\tilde{r}_{\text{thresh}} = 0.5$ [rad].

4. Simulations

The simulations were performed in Matlab/Simulink using a nonlinear six-degrees-of-freedom model of an aircraft controlled by its autopilot described by Ducard (2009). The aircraft is flying straight, at a constant level and at a constant speed of 30 m/s. These conditions correspond to difficult circumstances for an FDI system due to the lack of excitation. The actuator fault scenario consists of the failure of Aileron 1 at a small deflection of 1 deg during the time interval $[10 \ldots 40\,\text{s}]$, the failure of aileron 2 that gets also stuck at 1 deg during $[70 \ldots 100\,\text{s}]$, the rudder stucks at -1 deg during $[130 \ldots 160\,\text{s}]$, Elevator 1 gets stuck at 2 deg during $[190 \ldots 220\,\text{s}]$, and finally Elevator 2 also stucks at 2 deg during $[250 \ldots 280\,\text{s}]$.

Simulations were carried out with Gaussian sensor noise with zero mean and a standard deviation as summarized in Table 1. Moreover, uncertainties (in the aircraft model used in the prediction step of the EKF

Table 1. Sensor-suite description and accuracy.

Sensor	Description	Standard Deviation
Gyrometers	Angular velocity	$\sigma_{p,q,r}$ = 0.08 rad/s
Pitot Tube	Airspeed	σ_{V_T} = 5 m/s
Flow vane	Angle of attack	σ_α = 0.049 rad
Flow vane	Sideslip angle	σ_β = 0.049 rad

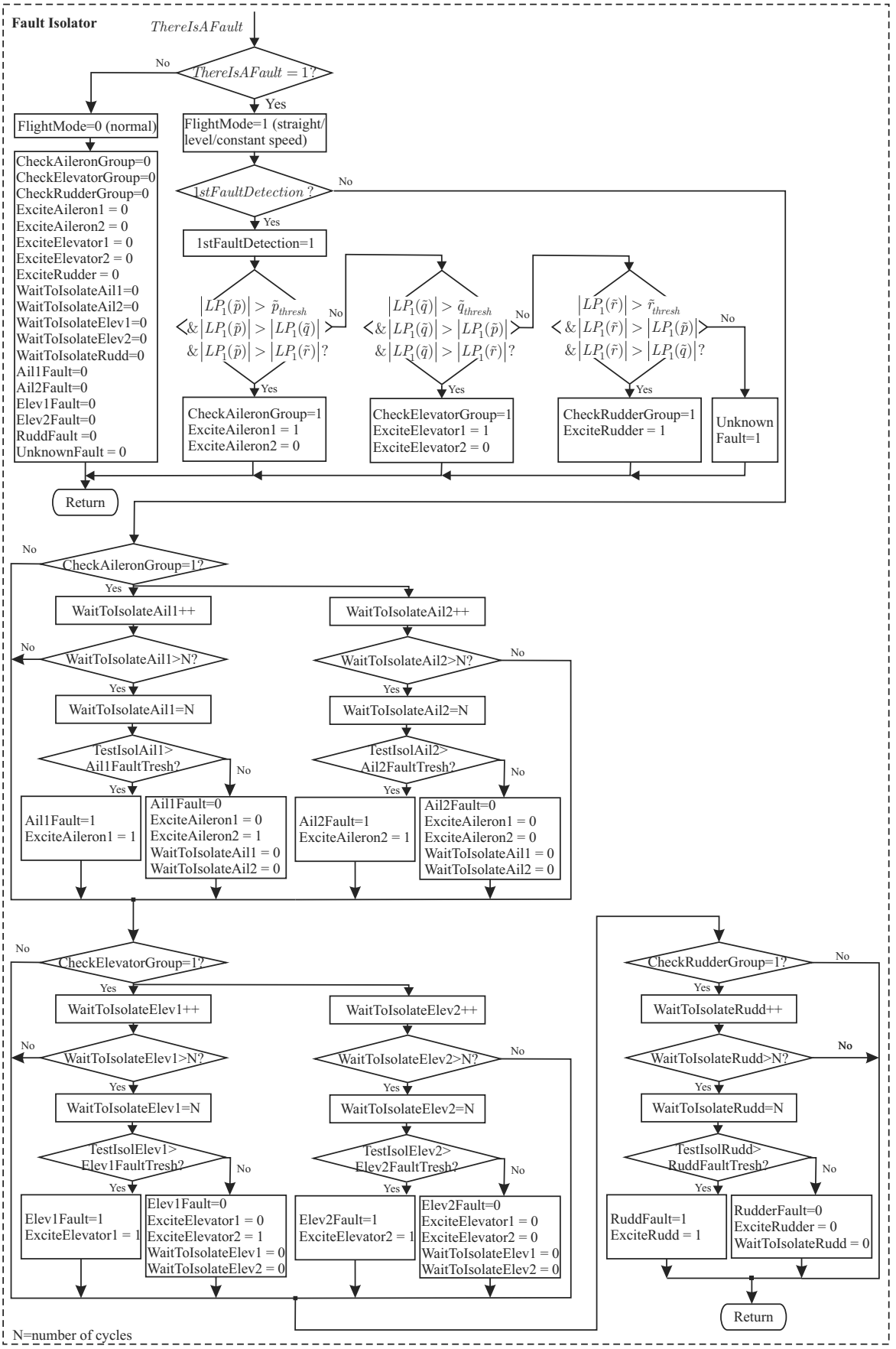

Fig. 6. Architecture of the fault isolator subsystem.

in the SMAC-FDI system) are introduced in the form of reducing by 25% the values of the torque vector $[L, M, N]^\top$ involved in Eqn. (1). This is similar to taking an underestimated value of the model input coefficient $\hat{b}_\chi$ used in Section 3.2.3, and it corresponds to a worse case scenario in terms of the FDI performance, than if the coefficient $\hat{b}_\chi$ had been overestimated, as explained in Remark 1 in Section 3.2.3. This simulation scenario is chosen to show the capability of the SMAC-FDI system (i) to detect actuator failure even if the angle of the stuck control surface is very small, and (ii) to distinguish the precise location of an actuator failure despite the ambiguity that may arise due to actuator redundancies in the system. It is indeed shown by Ducard and Geering (2008) how, e.g., the MMAE or the EMMAE FDI scheme performs poorly to isolate a failed actuator between two actuators having the same aerodynamic effect on the aircraft. SMAC-FDI is run in simulation at a rate of 50 Hz. Figure 7 shows that the SMAC-FDI detects the presence of the fault after at most 1 s.

Figure 10 shows that the isolation of a faulty actuator takes at maximum about 4 s and the detection of a fault removal is detected in all cases in less than 2 s. Figures 8 and 9 show the actuator control signals and the results of the AHE subsystem, respectively. Finally, Fig. 10 shows the satisfactory diagnostic results of the isolator subsystem.

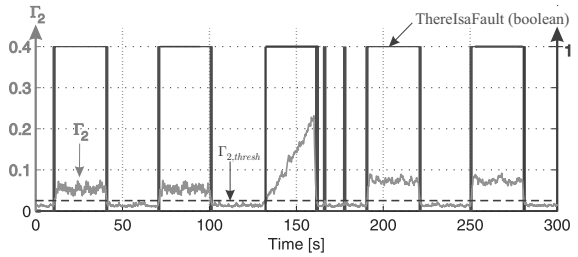

Fig. 7. Results of the fault detector: Boolean variable "ThereIsaFault" in black, and the grey curve is the signal Γ_2 in [rad]. The threshold value is $\Gamma_{2,\mathrm{thresh}} = 0.025$ [rad/s].

The approach is also tested in the presence of a significant wind disturbance. A Dryden wind model is used to generate wind gusts, with velocities up to 25% of the aircraft cruising speed (30 m/s). For wind conditions weaker than those shown in Fig. 11, the FDI results are those of Fig. 10. However, for wind conditions equal or stronger than those shown in Fig. 11, an accurate diagnosis becomes more challenging as shown in Fig. 12.

First, at $t = 31$ s and $t = 106$ s, two short glitches in the SMAC-FDI diagnosis appear. At $t = 250$ s, the left elevator is declared faulty when it is actually the right one that is faulty, because the wind masks the effects of artificial exciting signals for some time. However, in all cases, the correct faulty-actuator group is detected and no

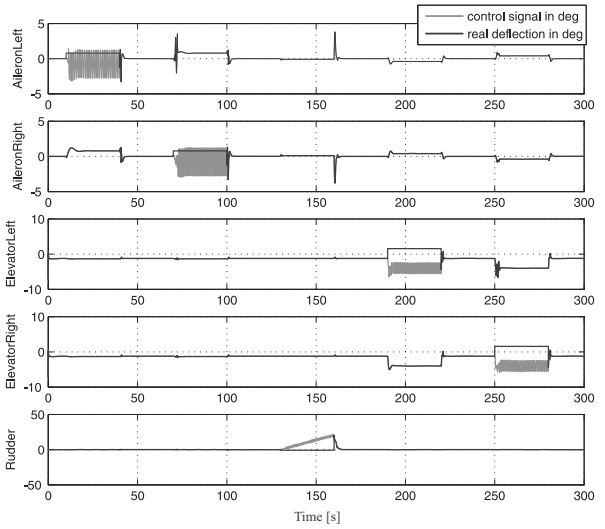

Fig. 8. Control signals (in [deg]) of the actuators during the sequence of failures.

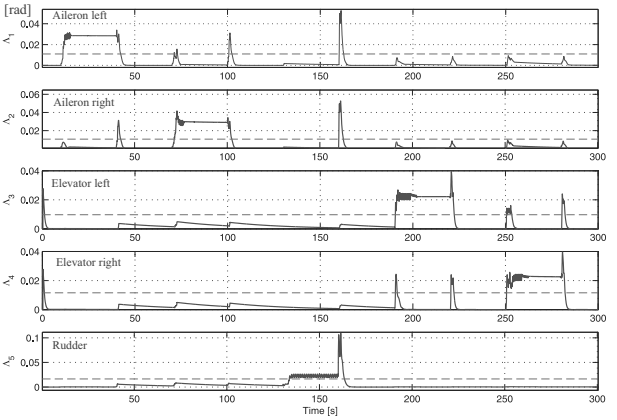

Fig. 9. Results of the actuator health evaluator subsystem. The dashed line is $\Lambda_{\mathrm{thresh}} = 0.01$ [rad].

false alarm is triggered despite the external disturbance. A possible solution, in windy conditions, is to retune some thresholds and enlarge the time allowed to the FDI system to make a decision on whether and which actuator should be declared failed.

5. Properties of the SMAC-FDI system

The benefits of the SMAC-FDI system are the following:

- It is able to detect the presence of an actuator fault, using a single EKF for residual generation with only three state elements, p, q, r. It is of low computational load (no need for a bank of EKFs) and could be implemented on a small microcontroller.

- Fault isolation is based on an active and systematic actuator testing procedure, thus reducing isolation

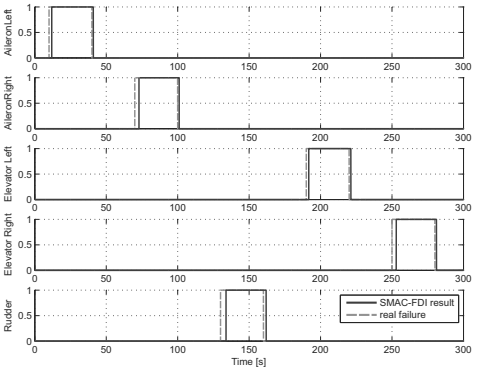

Fig. 10. Diagnostic results of the fault isolator: 0 means no fault, 1 means an actuator fault.

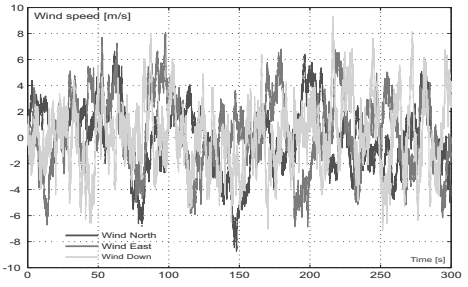

Fig. 11. Wind gusts used in the simulations to test the robustness of SMAC-FDI.

latencies, removing isolation ambiguities among equivalent actuators and increasing the robustness of this FDI method against external perturbations and model uncertainties. However, significant wind gusts may shortly contribute to trigger false alarms or mask the artificial exciting signals for some time, thus the approach here could be retuned or adapted online when windy conditions arise.

- The SMAC-FDI system is well suited for locked- or floating-actuator failure type. It is scalable to a larger number of actuators and can deal with simultaneous faults. It is easy to tune, and it does not require any additional sensors.
- The isolation process is insensitive to the control signals' amplitude, contrary to methods based on residuals. However, the fault isolation process works best if during this phase the aircraft is commanded to fly straight and at a given level.
- The SMAC-FDI system can also track a fault once detected even with low natural excitation.

5.1. Discussion of computational load requirements. The SMAC-FDI algorithm automatically reduces to the minimum amount of computation required. Indeed, the fault isolator is disabled when the flag ThereIsaFault=0

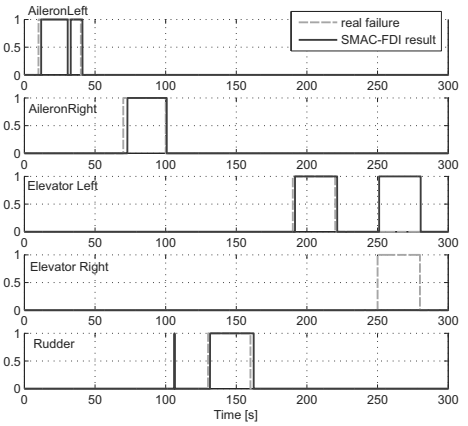

Fig. 12. Diagnostic results in the windy conditions of Fig. 11: 0 means no fault, 1 means actuator fault.

and enabled when ThereIsaFault=1. On the other hand, in an MMAE or an EMMAE structure, the whole bank of $N + 1$ EKFs (with at least six states) is constantly running to monitor N actuators. The MMAE method is even more computationally intensive. In SMAC-FDI, the computational load is considerably reduced since only one EKF is constantly running with only three states which are actually sufficient for FDI purposes. Most other FDI methods require additional state elements in their state vector. In addition, most of them focus on residuals at the system's output, whereas in this new scheme the output residuals on the turn rates only serve to detect the presence of a fault and the flight controller's output is used to isolate the fault. Therefore, SMAC-FDI is a very fast method and well suited for a small microcontroller.

6. Conclusion and outlook

This FDI system is based on a single-model EKF filter that generates residuals as soon as the behavior of the aircraft deviates from expected. If a fault is detected, the aircraft is commanded to fly straight and at a given level. A procedure is engaged to systematically excite each suspected actuator and decide whether it is failed. The isolation process is done by observing the control signals. The tuning of this FDI system is shown and is quite straightforward. The paper presented successful detection and isolation during a sequence of actuator failures and recoveries in no or moderate wind disturbances. For higher wind disturbances, the performance of the fault diagnosis degrades, and future works will address this issue, in particular by adapting, during the flight, some parameters involved in different thresholds of the proposed FDI system (for example, thresholds Γ_2 and $\Lambda_{\mathrm{thresh}}$), depending on the flight and wind conditions.

References

Alwi, H., Edwards, C. and Tan, C.P. (2011). *Fault Detection and Fault Tolerant Control Using Sliding Modes*, Springer-Verlag, London.

Athans, M. (1977). The stochastic control of the F-8c aircraft using a multiple model adaptive control (MMAC) method, Part I: Equilibrium flight, *IEEE Transactions on Automatic Control* **22**(5): 768–780.

Azam, M., Pattipati, K., Allanach, J., Poll, S. and Petterson-Hine, A. (2005). In-flight fault detection and isolation in aircraft flight control systems, *Proceedings of the IEEE Aerospace Conference, Big Sky, MT, USA,* paper 1429.

Bateman, F., Noura, H. and Ouladsine, M. (2011). Active fault diagnosis and major actuator failure accommodation: Application to a UAV, *in* A. Balint (Ed.), *Advances in Flight Control Systems*, InTech, Rijeka, pp. 135–158.

Belcastro, C. and Chang, B.-C. (2002). Uncertainty modeling for robustness analysis of failure detection and accommodation systems, *Proceedings of the IEEE American Control Conference, Anchorage, AK, USA*, pp. 4776–4782.

Benini, B., Castaldi, P. and Simani, S. (2009). *Fault Diagnosis for Aircraft System Models: An Introduction from Fault Detection to Fault Tolerance*, VDM Verlag Dr. Muller, Saarbrucken.

Blanke, M., Kinnaert, M., Lunze, J. and Staroswiecki, M. (2006). *Diagnosis and Fault Tolerant Control*, Springer Verlag, London.

Bonfè, M., Castaldi, P., Mimmo, N. and Simani, S. (2011). Active fault tolerant control of nonlinear systems: The cart-pole example, *International Journal of Applied Mathematics and Computer Science* **21**(3): 441–455, DOI: 10.2478/v10006-011-0033-y.

Boskovic, J.D., Redding, J. and Mehra, R.K. (2007). Robust fault tolerant flight control using a new failure parameterization, *Proceedings of the IEEE American Control Conference, New York, NY, USA*, pp. 5753–5758.

Brown, R.G. and Hwang, P.Y.C. (1997). *Introduction to Random Signals and Applied Kalman Filtering*, John Wiley & Sons, New York, NY.

Campbell, M.E., Lee, J.W., Scholte, E. and Rath Bun, D. (2007). Simulation and flight test of autonomous aircraft estimation, planning, and control algorithms, *AIAA Journal of Guidance, Control, and Dynamics* **30**(6): 1597–1609.

Campbell, S.L. and Nikoukhah, R. (2004). *Auxiliary Signal Design for Failure Detection*, Princeton University Press, Princeton, NJ.

Castaldi, P., Geri, W., Bonfè, M., Simani, S. and Benini, M. (2010). Design of residual generators and adaptive filters for the FDI of aircraft model sensors, *Control Engineering Practice* **18**(5): 449–495, DOI:10.1016/j.conengprac.2008.11.006.

Chen, J. and Patton, R.J. (1999). *Robust Model-Based Diagnosis for Dynamic Systems*, Kluwer Academic, Boston, MA.

Ducard, G. (2009). *Fault-tolerant Flight Control and Guidance Systems: Practical Methods for Small Unmanned Aerial Vehicles*, Advances in Industrial Control, Springer-Verlag, London.

Ducard, G. (2013). The SMAC fault detection and isolation scheme: Discussions, improvements, and application to a UAV, *Proceedings of the IEEE 2013 Conference on Control and Fault Tolerant Systems (SysTol'13), Nice, France*, pp. 480–485.

Ducard, G. and Geering, H.P. (2006). A reconfigurable flight control system based on the EMMAE method, *Proceedings of the IEEE American Control Conference, Minneapolis, MN, USA*, pp. 5499–5504.

Ducard, G. and Geering, H.P. (2008). Efficient nonlinear actuator fault detection and isolation system for unmanned aerial vehicles, *AIAA Journal of Guidance, Control, and Dynamics* **31**(1): 225–237.

Ducard, G. and Geering, H.P. (2010). SMAC-FDI: New active fault detection and isolation scheme with high computational efficiency, *Proceedings of the IEEE 2010 Conference on Control and Fault Tolerant Systems, Nice, France*, pp. 30–37.

Eide, P. and Maybeck, P.S. (1996). An MMAE failure detection system for the F-16, *IEEE Transactions on Aerospace and Electronic Systems* **32**(3): 1125–1136.

Elgersma, M., Enns, D., Shald, S. and Voulgaris, P. (1998). Parameter identification for systems with redundant actuators, *Proceedings of the AIAA Guidance, Navigation and Control Conference and Exhibit, Boston, MA, USA*, pp. 109–117.

Elgersma, M. and Glavaski, S. (2001). Reconfigurable control for active management of aircraft system failures, *Proceedings of IEEE American Control Conference, Arlington, VA, USA*, pp. 2627–2639.

Fekri, S., Athans, M. and Pascoal, A. (2006). Issues, progress and new results in robust adaptive control, *International Journal of Adaptive Control and Signal Processing* **20**(10): 519–579.

Isermann, R. (2006). *Fault-Diagnosis Systems, An Introduction from Fault Detection to Fault Tolerance*, Springer-Verlag, Berlin/Heidelberg.

Magill, D.T. (1965). Optimal adaptive estimation of sampled stochastic processes, *IEEE Transactions on Automatic Control* **10**(4): 434–439.

Maybeck, P.S. (1999). Multiple model adaptive algorithms for detecting and compensating sensor and actuator/surface failures in aircraft flight control systems, *International Journal of Robust and Nonlinear Control* **9**(14): 1051–1070.

Maybeck, P.S. and Stevens, R.D. (1991). Reconfigurable flight control via multiple model adaptive control methods, *IEEE Transactions on Aerospace and Electronic Systems* **27**(3): 470–479.

Möckli, M. (2006). *Guidance and Control for Aerobatic Maneuvers of an Unmanned Airplane*, Ph.D. thesis, Diss. No. 16586, ETH Zurich, Zurich.

Patton, R.J. and Chen, J. (1997). Observer-based fault detection and isolation: Robustness and applications, *Control Engineering Practice* **5**(5): 671–682.

Patton, R.J., Uppal, F.J., Simani, S. and Polle, B. (2008). Reliable fault diagnosis scheme for a spacecraft control system, *Journal of Risk and Reliability* **222**(2): 139–152, DOI: 10.1243/1748006XJRR98.

Rodrigues, M., Theilliol, D., Aberkane, S. and Sauter, D. (2007). Fault tolerant control design for polytopic LPV systems, *International Journal of Applied Mathematics and Computer Science* **17**(1): 27–37, DOI:10.2478/v10006-007-0004-5.

Simani, S., Fantuzzi, C. and Patton, R. (2003). *Model-Based Fault Diagnosis in Dynamic Systems Using Identification Techniques*, Advances in Industrial Control, Springer-Verlag, London.

Tanaka, N., Suzuki, S., Masui, K. and Tomita, H. (2006). Restructurable guidance and control for aircraft with failures considering gusts effects, *AIAA Journal of Guidance, Control, and Dynamics* **29**(3): 635–642.

Theilliol, D., Join, C. and Zhang, Y. (2008). Actuator fault tolerant control design based on a reconfigurable reference input, *International Journal of Applied Mathematics and Computer Science* **18**(4): 553–560, DOI:10.2478/v10006008-0048-1.

Zhang, Y. and Jiang, J. (2000). Integrated design of reconfigurable fault-tolerant control systems, *AIAA Journal of Guidance, Control, and Dynamics* **24**(1): 133–136.

Guillaume J.J. Ducard received his Master's degree in electrical engineering from ETH Zurich in 2004. He completed his doctoral work in 2007 at ETH Zurich on fault-tolerant control for unmanned aerial vehicles. During his post-doc (2008–2009), he contributed to the famous flying machine arena at ETHZ with flight controllers for quadrocopters. Since the end of 2009, he has been an assistant professor at the University of Nice Sophia Antipolis, France. He focuses on nonlinear control and state estimation for UAVs.

Appendix

Table A1. Aircraft model parameters

Parameter	Value	Definition
$\boldsymbol{I}^b$ [kg·m^2]	$\begin{bmatrix} 2.56 & 0 & 0.5 \\ 0 & 10.9 & 0 \\ 0.5 & 0 & 11.3 \end{bmatrix}$	airplane inertia matrix
S [m^2]	1.80	wing surface
$\bar{c}$ [m]	0.58	mean aerodynamic chord
b [m]	3.1	wing span
C_{Z1}	1.29×10^{-2}	lift derivative
$C_{Z\alpha}$	-3.25	lift derivative
C_{X1}	-2.12×10^{-2}	drag derivative
$C_{X\alpha}$	-2.66×10^{-2}	drag derivative
C_{Y1}	-3.79×10^{-1}	side force derivative
$C_{L_{a1}} = -C_{L_{a2}}$	-3.395×10^{-2}	roll derivative
$C_{L_{e1}} = -C_{L_{e2}}$	-0.485×10^{-2}	roll derivative
$C_{L\beta}$	-1.30×10^{-2}	roll derivative
$C_{L\bar{p}}$	-1.92×10^{-1}	roll derivative
$C_{L\bar{r}}$	3.61×10^{-2}	roll derivative
C_{M1}	2.08×10^{-2}	pitch derivative
C_{Me}	5.45×10^{-1}	pitch derivative
$C_{M_{e1}} = C_{M_{e2}}$	2.725×10^{-1}	pitch derivative
$C_{M_{a1}} = C_{M_{a2}}$	0.389×10^{-1}	pitch derivative
$C_{M\alpha}$	-9.03×10^{-2}	pitch derivative
$C_{M\bar{q}}$	-9.83	pitch derivative
$C_{N_{\delta_r}}$	5.34×10^{-2}	yaw derivative
$C_{N\beta}$	8.67×10^{-2}	yaw derivative
$C_{N\bar{r}}$	-2.14×10^{-1}	yaw derivative

Received: 20 February 2014
Revised: 8 September 2014